

Detailed modeling of the statistical uncertainty of Thomson scattering measurements

This content has been downloaded from IOPscience. Please scroll down to see the full text.

[View the table of contents for this issue](#), or go to the [journal homepage](#) for more

Download details:

IP Address: 128.104.166.143

This content was downloaded on 13/12/2013 at 19:25

Please note that [terms and conditions apply](#).

RECEIVED: September 4, 2013

ACCEPTED: October 24, 2013

PUBLISHED: November 6, 2013

16th INTERNATIONAL SYMPOSIUM ON LASER-AIDED PLASMA DIAGNOSTICS,
22–26 SEPTEMBER 2013,
MADISON, WISCONSIN, U.S.A.

Detailed modeling of the statistical uncertainty of Thomson scattering measurements

L.A. Morton,¹ E. Parke and D.J. Den Hartog

*Department of Physics, University of Wisconsin,
1150 University Avenue, Madison WI, U.S.A.*

E-mail: lamorton@wisc.edu

ABSTRACT: The uncertainty of electron density and temperature fluctuation measurements is determined by statistical uncertainty introduced by multiple noise sources. In order to quantify these uncertainties precisely, a simple but comprehensive model was made of the noise sources in the MST Thomson scattering system and of the resulting variance in the integrated scattered signals. The model agrees well with experimental and simulated results. The signal uncertainties are then used by our existing Bayesian analysis routine to find the most likely electron temperature and density, with confidence intervals.

In the model, photonic noise from scattered light and plasma background light is multiplied by the noise enhancement factor (F) of the avalanche photodiode (APD). Electronic noise from the amplifier and digitizer is added. The amplifier response function shapes the signal and induces correlation in the noise. The data analysis routine fits a characteristic pulse to the digitized signals from the amplifier, giving the integrated scattered signals. A finite digitization rate loses information and can cause numerical integration error.

We find a formula for the variance of the scattered signals in terms of the background and pulse amplitudes, and three calibration constants. The constants are measured easily under operating conditions, resulting in accurate estimation of the scattered signals' uncertainty. We measure $F \approx 3$ for our APDs, in agreement with other measurements for similar APDs. This value is wavelength-independent, simplifying analysis. The correlated noise we observe is reproduced well using a Gaussian response function. Numerical integration error can be made negligible by using an interpolated characteristic pulse, allowing digitization rates as low as the detector bandwidth. The effect of background noise is also determined.

KEYWORDS: Detector alignment and calibration methods (lasers, sources, particle-beams); Plasma diagnostics - interferometry, spectroscopy and imaging; Analysis and statistical methods

¹Corresponding author.

Contents

1	Introduction and motivation	1
2	Model of detector system and noise sources	2
3	Simulation results	2
3.1	Constant signal model	2
3.2	Pulse photonic noise	3
3.3	Numerical integration error	3
3.4	Background noise	5
4	Experimental results	6
4.1	AC and DC response functions	6
4.2	Constant signal model	7
4.3	Pulsed signal model	8
5	Typical electron temperature uncertainties	9
6	Conclusion	9

1 Introduction and motivation

In this paper, we analyze the sources of statistical uncertainty in the the electron temperature measurements made using a polychromator-based Thomson scattering (TS) system with avalanche photodiode (APD) detectors. Such TS diagnostics are a widely used and reliable way to determine the electron temperature and density of laboratory plasmas. The Madison Symmetric Torus (MST) TS system uses filter polychromators with avalanche photodiode (APD) detectors to capture the scattering spectrum. The analysis code takes the integral of the pulse corresponding to the scattered light in the digitized signal from each detector. The electron temperature and density are derived by fitting the scattering spectrum to the integrated signals. For more information on the MST TS system see [1–4].

The main sources of noise in such a system are electronic and photonic noise occurring in the APD detectors. APD noise has been well-characterized by simple models [5–9]. This paper focuses on how the noise translates into uncertainty in the scattered signals, through the interaction of the noise sources, the shape of the scattered pulse, the amplifier properties, the digitization rate, and the numerical integration method. The final step, finding the uncertainty of the electron temperature and density based on the scattered signal uncertainty, is already implemented for the MST TS system using a Bayesian statistical method. [10]

2 Model of detector system and noise sources

For the complete derivation of this model, refer to the supplementary material. Poisson-distributed photons are absorbed by the APD, producing primary electrons. The avalanche process multiplies the number of electrons and also increases the noise. The current from the APD is converted to an output voltage by an amplifier/filter. The digitized signal $s(t_i)$ is numerically integrated over the scattered signal pulse to give the scattered signal S . These results assume that the integral is computed by χ^2 fitting of a ‘characteristic pulse,’ produced by averaging many observed pulses, to the digitized signal to estimate the pulse amplitude. There are three different types of uncertainty which influence the resulting value of S :

$$\text{Var}(S) = \varepsilon^2 \cdot S^2 + \frac{R^{-1}}{\tanh(R^{-1})} GMF \cdot S + (GMFr_{bg} + v_{\text{electr}}^2) \cdot \tau_{\text{int}}. \quad (2.1)$$

The term quadratic in S corresponds to numerical integration error, where ε is the relative error introduced by the integration method. It depends on the integration method, the digitizer sampling rate, and the shape of the output pulse. It may be reduced by using an interpolated characteristic pulse (see section 3.3).

The linear term arises from the Poisson statistics of the scattered photons, $\text{Var}(N_{ph}) = \langle N_{ph} \rangle$. G is gain of the amplifier, in V·s/electron. M is the avalanche multiplication factor of the APD, and F is the noise enhancement factor [6]. $R = B_{\text{digi}}/B_{\text{amp}}$ is the ratio of the digitizer bandwidth to the amplifier bandwidth. The correlation factor $R^{-1}/\tanh(R^{-1})$ expresses the diminishing returns of increasing the digitizer bandwidth beyond the bandwidth of the amplifier.

The constant term contains all the background noise sources, including the background plasma light (expressed in terms of the output signal voltage r_{bg}) and electronic noise v_{electr}^2 . Both contributions are power spectral densities in V²/Hz, and they are accumulated over the effective integration time τ_{int} , which depends on pulse shape and integration method.

3 Simulation results

Here we compare different aspects of the above analytical results to data from a Monte Carlo simulation of the same underlying model. In all simulations, photons (pulse and background) were drawn according to a Poisson distribution at 0.1 ns intervals, the resulting time-series was convolved with the amplifier response function, and the output pulse was fitted with a characteristic pulse (average of many output pulses) to find the inferred number of photons. These simulations do not model the avalanche multiplication process: $GMF \equiv 1$.

3.1 Constant signal model

We begin by testing equation (3.1), which gives the variance of the output signal $s(t)$ from the amplifier, given a constant source of background light which produces an average output signal $\langle s(t) \rangle$:

$$\text{Var}(s(t)) = GMFB_{\text{amp}} \langle s(t) \rangle \quad (3.1)$$

The bandwidth is defined to be:

$$B_{\text{amp}} = \frac{\int_0^\infty w^2(t) dt}{[\int_0^\infty w(t) dt]^2}, \quad (3.2)$$

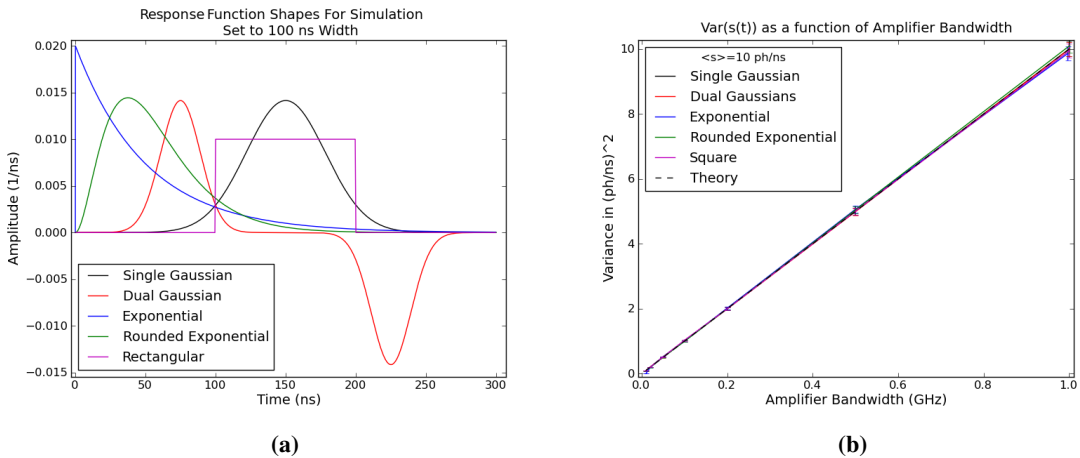


Figure 1. (a) Response function shapes used in the simulations. The ‘Rounded Exponential’ has the form $t^2 e^{-t/\tau}$. Response functions have $\tau_{\text{amp}} = 100$ ns in this plot. The ‘Dual Gaussian’ is motivated by the MST TS amplifiers (section 4.1). (b) The variance of $s(t)$ obeys $\text{Var}(s) = \text{GMF} \langle s \rangle \cdot B_{\text{amp}}$ over two orders of magnitude in B_{amp} . The input signal had $\langle s(t) \rangle = 10$ ph/ns. B for the ‘Dual Gaussian’ shape was calculated from the absolute value of the response function.

where $w(t)$ is the amplifier response function. Sample traces were simulated using the amplifier response functions shown in figure 1a, and the variance $Var(s(t))$ was computed. Figure 1b shows that the model agrees with the simulation for all the pulse shapes and over two orders of magnitude in B_{amp} .

3.2 Pulse photonic noise

We now verify the relation of the photonic noise from pulsed signals, the linear term in equation (2.1): $\text{Var}(S) = \frac{R}{\tanh(R)} \text{GMF} \cdot S$. For this section, the background photon rate in the simulation was very low (0.001 ph/ns) and the pulse arrival time was fixed, to eliminate numerical error ($\varepsilon = 0$). We used two response functions, ‘AC’ and ‘DC,’ designed to mimic the behavior of our system (see section 4.1 for details). Figure 2 shows that the agreement between simulation and theory is again excellent, with the variance scaling with the signal amplitude as expected for Poisson statistics. We also investigated the dependence of the signal variance on the ratio of digitizer to amplifier bandwidth. The model was derived specifically for an exponential response function (decaying exponential), and assuming that the input pulse is very broad compared to the response function. Figure 3 shows that the model gives a good estimate of the actual behavior for a variety of different response function shapes, and for narrow input pulse widths.

3.3 Numerical integration error

We next explore how the quadratic term in equation (2.1), the numerical integration error $\text{Var}(S) = \varepsilon^2 S^2$, depends on pulse shape and characteristic pulse resolution. The pulse arrival time is allowed to vary randomly in 0.1 ns steps to produce the integration error. Figure 4a illustrates the quadratic dependence characteristic of integration error. The error ε is inversely proportional to the interpolation ratio $R_{\text{interp}} \equiv \frac{\Delta_{\text{digi}}}{\Delta t_{\text{char.pulse}}}$ in figure 4b. The coefficient depends rather strongly on the pulse

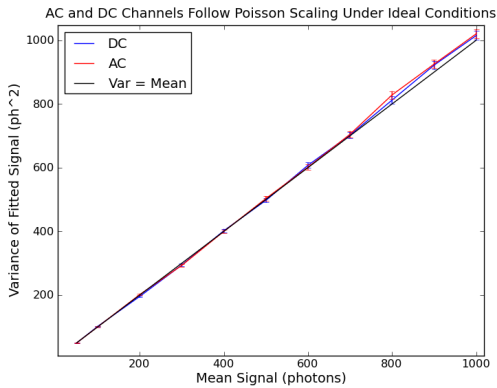


Figure 2. Simulated variance for pulse-fitting method agrees very well with theoretical prediction. The scattered light pulse was a Gaussian of width 17.7 ns. The correlation factor $R^{-1}/\tanh(R^{-1}) \approx 1$ here due to the high digitization rates. Error bars are standard error from 10,000 trials.

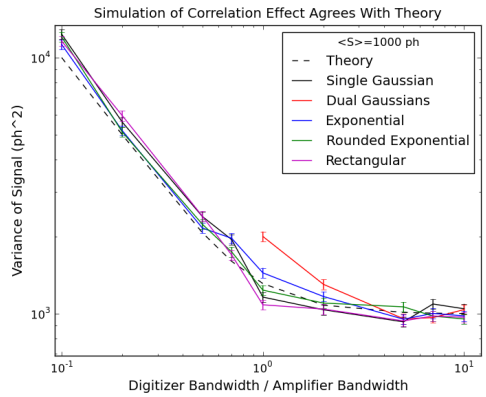
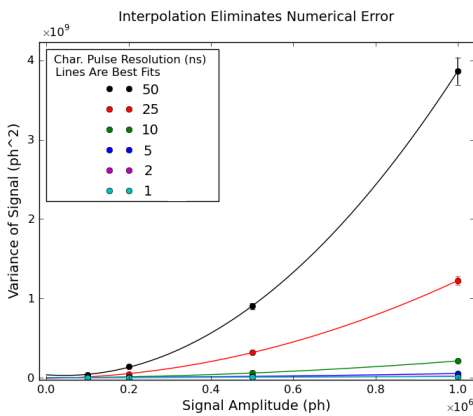
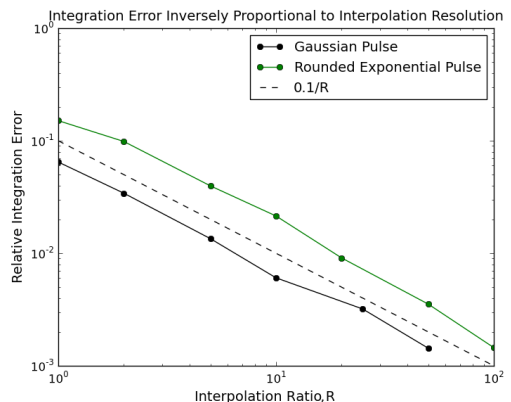


Figure 3. The amplifier bandwidth (determined from the response function) sets the minimum digitizer bandwidth necessary to achieve photon-limited uncertainty. The input was a Gaussian pulse (width 20 ns), the digitization rate was 100 MS/s, and the width of each response function was varied. The Dual Gaussian response function simulation breaks down for $R < 1$.



(a)



(b)

Figure 4. (a) The variance of fitted signal increases quadratically with mean signal amplitude due to numerical integration error. The sampling period was 100 ns, the input pulse width was 200 ns, and the interpolating characteristic pulse had a resolution of 1 to 50 ns. The amplifier response function was Gaussian with width 10 ns. (b) The relative error ϵ is inversely proportional to the resolution of the characteristic pulse.

shape. The ability to reduce the integration error by interpolated fitting relaxes a constraint on the digitizer. The digitization rate may be chosen to (marginally) satisfy $B_{\text{digi}} \geq B_{\text{amp}}$, provided the pulse is wide enough to be sampled by at least a few digitizer points.

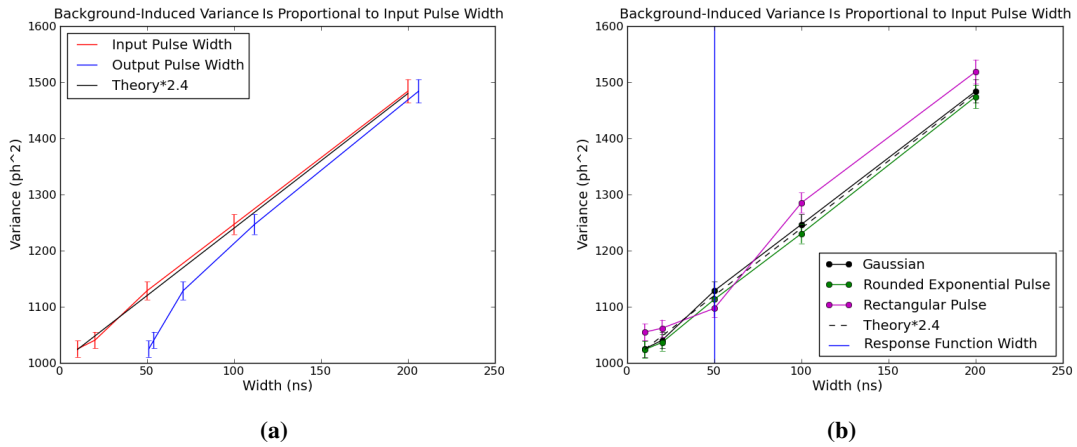


Figure 5. Background light should introduce additional variance to the pulse, proportional to $\tau_{\text{int}} \cdot N_{bg}$. The number of photons in the pulse was 1000, the background photon rate was 1 ph/ns and response function was a 50 ns Gaussian. (a) Plotting the variance against the input or output pulse width shows that variance is proportional to the input pulse width, although with a coefficient not predicted by the analytical results. (b) Different input pulse shapes share the same slope under the same conditions.

3.4 Background noise

We finally investigate the constant term in equation (2.1), the variance produced by background noise: $Var(S)_{bg} = GMF \langle r_{bg} \rangle \tau_{\text{int}}$, where τ_{int} is the width of the input pulse and r_{bg} is the output voltage corresponding to a constant input light source. The model assumes the input pulse is much longer than the response time of the amplifier, but the MST TS system operates in the regime where the two time scales are comparable. Thus, we investigated the effect of the amplifier response as well. In analogy with equation (3.2), the width of a function $f(t)$ was measured as:

$$\tau = \frac{[\int_0^\infty f(t)dt]^2}{\int_0^\infty f^2(t)dt}. \quad (3.3)$$

We plotted the variance from the simulation in two ways in figure 5a: against the input pulse width, and against the output pulse width. The variance is linear with the input pulse width, in agreement with theory; however, the slope is about 2.4 times the prediction. Figure 5b shows two other pulse shapes (square, and rounded exponential) share the same slope. This implies that the measure of the pulse width is consistently small, for unknown reasons.

According to the analytic results, which assumed an input pulse wider than the response function width, the response function width is irrelevant in calculating the effective background integration time. As illustrated in figure 6, simulations show that when the pulse is narrower than the response function, the response function width determines the background-induced variance. An interesting feature of the pulse-fitting method of integration is the breakdown at low signal-to-noise ratio. We illustrate this for the single and dual Gaussian pulse shapes by varying the pulse amplitude while holding the background photon rate fixed. Figure 7 shows that when the pulse arrival time is allowed to vary, the variance of the fitted signal jumps up significantly for low signal amplitudes. This is due to the loss of information about the location of the pulse in time.

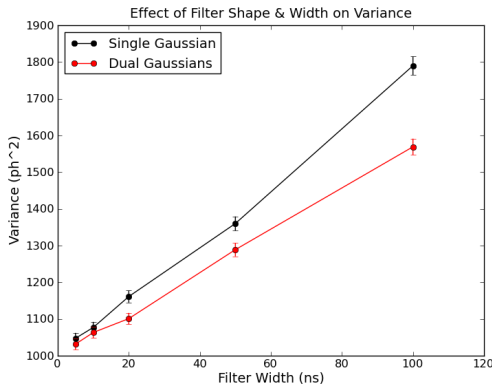


Figure 6. The background-induced variance is also proportional to the width of the response function. The input pulse was a 1.0 ns Gaussian. The background photon rate was 10 ph/ns, with 1000 photons in each pulse.

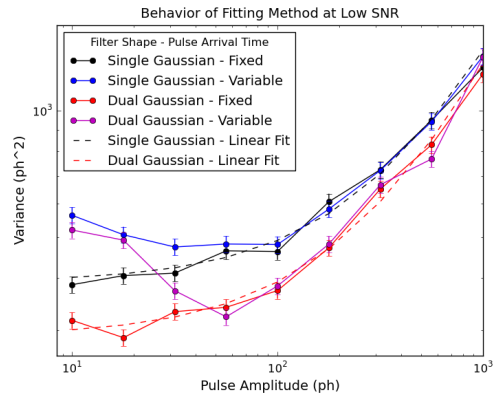


Figure 7. When the SNR of the data is low, the pulse location is not known precisely, and the fit quality degrades. Fixing the arrival time removes this behavior. The input pulse is a 10 ns Gaussian, the amplifier response function widths are all 50 ns, and the background rate is 10 ph/ns. The effective integration times are 39 ns (Single Gaussian) and 29 ns (Dual Gaussian).

4 Experimental results

In this section, we apply the model developed above to one of our reference APD detectors which has been absolutely calibrated. The MST TS diagnostic features C30956E Photodiodes from EC&G (formerly RCA). The amplifiers attached to them have two outputs: a directly coupled (DC) output channel which was intended for measuring the background plasma light level for the purposes of error analysis, and a high-pass-filtered (AC) output channel. The high-pass is accomplished by using a 100 ns delay line and a differential amplifier to cancel the background plasma light contribution on a fast time scale. We digitize the DC output at 100 MS/s, and the AC output at 1 GS/s. Since the bandwidth of both digitizers is more than sufficient, given the 25 MHz bandwidth of the APD/amplifier system, we are able to obtain scattered signal amplitudes from both outputs.

4.1 AC and DC response functions

The AC and DC response functions are characterized by the correlation function of the output,

$$\rho(t) = \frac{\text{Cov}[s(t'), s(t'+t)]}{\text{Var}[s(t')]} = \frac{\int_0^t w(t'-t)w(t')dt'}{\int_0^{t'} w^2(t')dt'} \quad (4.1)$$

The correlation functions for the AC and DC outputs with a constant light source input were obtained experimentally. The correlation functions were reproduced in simulations using single and dual Gaussian response functions, as shown in figure 8. The model AC and DC response functions were used for realistic simulations of the MST TS system.

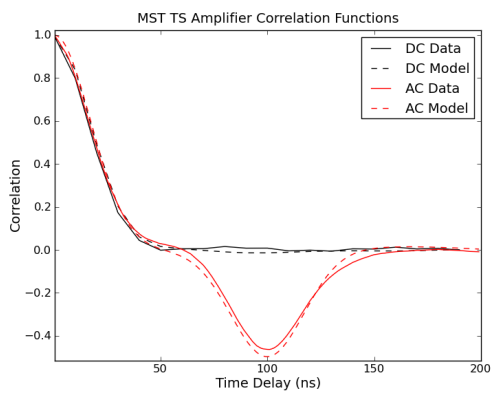


Figure 8. AC and DC correlation functions from experimental data and from simulations using model response functions. The model response functions were of type Single and Dual Gaussians as defined previously, with widths 42.5 and 85 ns respectively. The AC model had a delay of 100 ns between the positive & negative portions.

4.2 Constant signal model

We have also tested the dependence of the $\text{Var}(s(t))$ against $\langle s(t) \rangle$ using real data taken using a steady CW light source. From equation (3.1) our theoretical expectation for the DC output is that:

$$\text{Var}(s(t)) = GMFB_{\text{amp}} \langle s(t) \rangle.$$

However, the AC output is always zero under constant illumination, due to the symmetry of the response function. Therefore, we have plotted the variance of both the AC and DC signals against the DC mean signal in figure 9. The slope of the DC output corresponds to $G_{DC}MFB_{DC}$. We expect the AC slope to be $\frac{G_{AC}^2 B_{AC}}{G_{DC}^2 B_{DC}}$ times the DC slope. The intercept of each corresponds to $v_{\text{electr}}^2 B_{\text{amp}}$. The AC slope is 2.32 times the DC slope. $B_{AC}/B_{DC} = 1/2$ according to the modeled response functions. We measured $G_{AC}/G_{DC} = 2.15$ for a pulse. This yields a value of 2.31 for the ratio of the slopes, which is almost exactly what we observed.

F may be estimated from measured quantities. We inferred $G_{DC} \approx 3.3 \pm .2 \times 10^{-15} \text{ V}\cdot\text{s}/\text{e}$ from the absolutely calibrated gain $G_{\text{tot}} = GM\eta$ and an assumed value of $\eta = 0.8$ at 940 nm, using a measured $M \approx 90 \pm 1$. The DC amplifier bandwidth was estimated to be 23.5 MHz using equation (3.2) on the ‘DC’ model response function. Combining with the value of $\frac{\delta \text{Var}(s)}{\delta s} = 2.29 \times 10^{-5} \text{ V}$ from figure 9, the resulting value of $F = 3.2$ is near the values calculated for similar APDs by other Thomson scattering researchers [11, 12].

M and F are expected to be independent of wavelength for this type of APD which has a “reach-through” structure [13]. In order to verify this, the quantity $\text{Var}(s(t))/\langle s(t) \rangle = GMFB_{\text{amp}}$ was measured for constant input light signals using a monochromator with an incandescent lamp source. This quantity varied less than 5% over a range of wavelengths from 700 to 1064 nm.

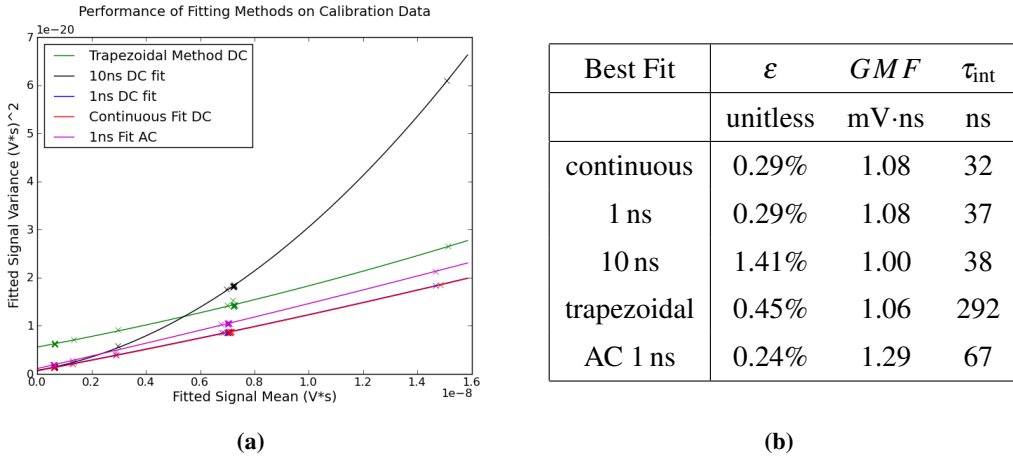


Figure 10. (a) Scaling of the integral variances with the integral mean, demonstrating the general quadratic form predicted by the model (b) Best-fit coefficients to the curves plotted in (a).

4.3 Pulsed signal model

If the digitizer bandwidth is large, so that the correlation correction factor $R^{-1}/\tanh(R^{-1})$ is unity, and there is no background light, equation (2.1) reads:

$$\text{Var}(S) = \varepsilon^2 \cdot S^2 + \text{GMF} \cdot S + v_{\text{electr}}^2 \cdot \tau_{\text{int}}$$

We tested this experimentally by varying the input pulse amplitude and integration method. We used a very reproducible pulsed diode source at 940 nm wavelength and 20 ns pulse length for these measurements. Amplitude fluctuations from the pulsed light source can result in a quadratic term which could obscure the integration error ε , so having a stable source is important. The linear term gives us a second measurement of GMF under pulsed operation, as opposed to the CW results in the preceding section. We also use v_{electr}^2 to infer τ_{int} from the constant term. We used four different integration methods for the DC output: trapezoidal rule, a standard characteristic pulse fitting method (10 ns time resolution); an interpolated pulse-fitting method (1 ns time resolution); and an analytic pulse fitting method. We also used 1 ns resolution pulse fitting on the AC output.

The results of the experiment are shown in figure 10a, where $\text{Var}(S)$ is plotted against S . Table 10b displays the best fit to the parameters in the model. The AC value of GMF has been corrected for the AC gain so it is comparable to the DC values. Notice that all DC methods agree on the value of GMF, but the AC channel has a larger value despite the gain correction. This must be due to error in measuring the AC or DC gain, since M and F must be the same since both channels share the same APD. The fitting methods have a much smaller effective integration time compared to the trapezoidal quadrature, since the quadrature was performed over a 320 ns window. The values of τ_{int} are rather smaller than expected given the width of the response functions. However this is not a sensitive test of the background contribution since the background is not varied. Fitting the characteristic pulse with 10 ns resolution to the DC channel displays more numerical error than the other methods, although it only becomes significant at large amplitudes (beyond the typical operating regime of our system). In the final analysis, the AC fitting method performs slightly worse than the interpolated DC fitting. The AC integration time is longer, which makes it more

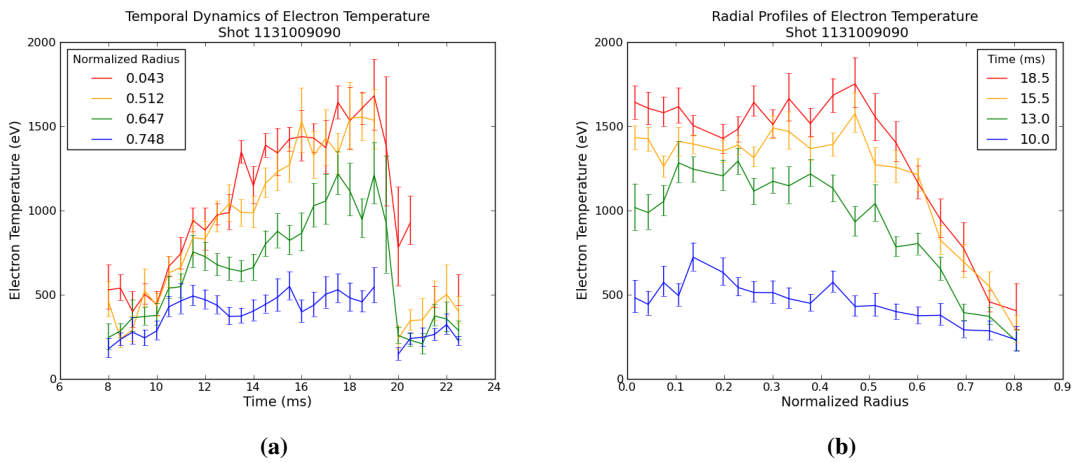


Figure 11. (a) Electron temperature as a function of discharge time, for 4 selected radial points. The discharge starts at $t = 0$ ms, and the improved confinement begins at 10 ms, and ends with a violent collapse at 19 ms. (b) The radial profile of electron temperature at 4 selected time points for the same shot.

sensitive to background noise (electronic or photonic) and it also has a larger GMF which makes it more sensitive to photonic noise in the pulse.

In section 4.2 we were able to find GMF using CW illumination, instead of a pulsed light source. We obtained for the DC channel $GMF = 0.95 \text{ mV}\cdot\text{ns}$ for the CW and $1.08 \text{ mV}\cdot\text{ns}$ from the pulsed case, showing 14% disagreement, which is reasonable given uncertainties. For the AC channel, the CW value of $GMF = 0.88 \text{ mV}\cdot\text{ns}$ is 32% smaller than the pulsed result, $1.29 \text{ mV}\cdot\text{ns}$. The AC channel results required more estimated quantities to obtain, which could explain the larger discrepancy.

5 Typical electron temperature uncertainties

Under typical operating conditions (laser energy of 2 Joules/pulse and moderate plasma background light) MST Thomson Scattering obtains average uncertainties of 10–15%, with best values of 5% or lower. Figure 11 shows data obtained from a recent improved confinement discharge, illustrating the scale of the uncertainties as compared to the temporal and spatial variations of the mean temperature throughout a discharge. The error bars represent 1σ confidence interval around the most probable temperature, found using the Bayesian procedure outlined in [10]. The temperature uncertainties are computed using the uncertainties in the scattered signals, which are themselves estimated using the model developed here, with coefficients determined from calibration. The MST TS system is not calibrated for absolute electron density measurements, so we have not considered the uncertainty in the electron density.

6 Conclusion

We have developed a simple but comprehensive model of all identified sources of uncertainty in the MST TS system, and how these uncertainties propagate to the uncertainty in the scattered spectrum. The model incorporates integration error, photonic noise from the scattered signal, and electronic

and photonic background noise. The noise becomes correlated due to the amplifier response function, and this is taken into account, along with digitization effects. The model is applicable to both quadrature and pulse-fitting methods for integration of the scattered signal. We have applied this model to experimental data gathered about our system, demonstrating that the model fits the data well and produces calibration coefficient values which are reasonable given prior knowledge.

Future efforts may be directed toward a more comprehensive model of the effect of the background noise on pulse-fitting, especially in the case where the plasma background light fluctuates. It would be worthwhile investigating experimentally the variance of the fitted pulse as a function of background light level, since this has not yet been done.

Acknowledgments

Thanks to L. Albantakis and W. C. Young for helpful proof-reading. This work is supported by the US Department of Energy.

References

- [1] H.D. Stephens, M.T. Borchardt, D.J. Den Hartog, A.F. Falkowski, D.J. Holly, R.O'Connell and J.A. Reusch, *Calibration of a thomson scattering diagnostic for fluctuation measurements, Rev. Sci. Instrum.* **79** (2008) 10E734.
- [2] H. Stephens, *Electron Temperature Structures Associated With Magnetic Tearing Modes in the Madison Symmetric Torus*, Ph.D. Thesis, University of Wisconsin, Madison, U.S.A. (2010).
- [3] J.A. Reusch, M.T. Borchardt, D.J. Den Hartog, A.F. Falkowski, D.J. Holly, R. O'Connell and H.D. Stephens, *Multipoint thomson scattering diagnostic for the madison symmetric torus reversed-field pinch, Rev. Sci. Instrum.* **79** (2008) 10E733.
- [4] E. Parke et al., *Improvements to the calibration of the mst thomson scattering diagnostic, Rev. Sci. Instrum.* **83** (2012) 10E324.
- [5] B.E.A. Saleh and M.C. Teich, *Fundamentals of Photonics*, Wiley, 2nd edition (2007).
- [6] P.P. Webb, R.J. McIntyre and J. Conradi, *Properties of Avalanche Photodiodes, RCA Review* **35** (1974) 234.
- [7] F. Laforce, *Low noise optical receiver using si apd, Proc. SPIE* **7272** (2009) 721210.
- [8] Solid State Division, *Characteristics and use of si apd (avalanche photodiode)*, Technical report, Hamamatsu.
- [9] L. Jiangui, A. Fremout, P. Bruyndonckx, S. Tavernier, J.-F. Loude and C. Morel, *Evaluation of different types of avalanche photo diodes from hamamatsu and perkin-elmer, IEEE Nucl. Sci. Conf. R.* **2** (2001) 873.
- [10] R. O'Connell, D.J. Den Hartog, M.T. Borchardt, D.J. Holly, J.A. Reusch and H.D. Stephens, *Optimizing a thomson scattering diagnostic for fast dynamics and high background, Rev. Sci. Instrum.* **79** (2008) 10E735.
- [11] F. Orsitto, A. Brusadin and E. Giovannozzi, *Avalanche photodiodes operating parameter optimization for the frascati tokamak upgrade thomson scattering system, Rev. Sci. Instrum.* **68** (1997) 1201.
- [12] D.W. Johnson, B.P. LeBlanc, D.L. Long and G. Renda, *Apd detector electronics for the nstx thomson scattering system, Rev. Sci. Instrum.* **72** (2001) 1129.
- [13] Photodiode c30954e, c30955e, c30956e data sheet: large area long wavelength enhanced silicon avalanche photodiodes for general-purpose applications.